

Effect of the Addition of CeO₂ on the Microstructure and Corrosion of in-situ TiB/Ti Composite Coatings Prepared by Laser Cladding Technology

Guangyu Han¹, Youfeng Zhang^{1,*}, Bo wang¹, Zhixiao Zhang²

¹ School of Materials Engineering, Shanghai University of Engineering Science, Shanghai 201620, China

² Department of Materials Science and Engineering, National University of Singapore, Singapore 117574, Singapore

*E-mail: zhangyoufeng@sues.edu.cn

Received: 10 March 2020 / Accepted: 22 November 2020 / Published: 31 December 2020

Ti alloy coating is a common composite coating. However, a few studies focus on the corrosion resistance of the coatings. Herein, TiB composite coatings were successfully fabricated on the surface of a Ti-6Al-4V alloy with TiB/CeO₂ powders by *in situ* laser cladding technology, and the microstructure and corrosion resistance were investigated. The cladding coating and the substrate metallurgically combined well after laser cladding treatment. The coatings consisted of TiB and α -Ti phase. The addition of CeO₂ contributed to the formation of a uniform and refined microstructure of the cladding coatings. The microhardness of the cladding coating was improved, and it is threefold to fourfold higher than that of the substrate when the addition of CeO₂ was 3 wt%. The corrosion properties were significantly improved. Electrical impedance spectroscopy and polarization tests showed that the corrosion resistance of the cladding coatings with 3 wt% CeO₂ was better than those of other samples. All samples exhibited an obvious near-capacitive behaviour after immersion in a corrosive medium.

Keywords: Laser cladding; Ti-6Al-4V alloy; CeO₂; microhardness; corrosion resistance

1. INTRODUCTION

Ti and Ti alloys have been widely used in aviation, aerospace, chemical and biomedical fields because they have excellent fatigue properties and biological compatibility. However, little attention has been paid to the application of Ti and Ti alloys in the marine industry due to the complicated corrosion and wear damage [7-10]. Based on the above-mentioned factors, many surface modification technologies have been adopted to improve the tribological and corrosion properties of Ti alloys. Amongst these surface modifications of Ti alloys, the laser cladding technology has attracted much attention [11-14].

This technology has many outstanding advantages as a method of surface treatment, such as the metallurgical combination between the cladding coating and the substrate of the Ti alloys, the rapid fabrication processing and the controllable components of the coatings [15-17].

Currently, rare-earth elements are suitable for addition into laser cladding coatings to achieve well-defined microstructures due to their appropriate physicochemical properties. For example, the electronic structure of such elements is unique, their atoms are highly mobile, and their ionic radius is large [18]. The addition of a suitable amount of a rare-earth element into cladding coatings can help refine their grains and improve their corrosion properties, oxidation resistance and wear resistance [19-27]. Consequently, several studies have been conducted on the addition of rare-earth compounds to cladding coatings, including La_2O_3 and Y_2O_3 [19, 21, 22, 24]. Nevertheless, research into the effect on the corrosion properties of the addition of CeO_2 to these laser cladding coatings is lacking. Zhang et al. [28] investigated the effects of CeO_2 on the microstructure and corrosion resistance of the TiC-VC reinforced Fe-based laser cladding layers; the cladding layer with the addition of 0.5 wt% CeO_2 exhibited an optimal corrosion resistance; subsequently, the inductive arc at low frequency was transformed into a capacitive arc.

TiB is also an excellent ceramic phase for the Ti-alloy composite coatings obtained using the laser cladding technology. The relevant research into Ti alloy coatings with TiB-reinforced particles mainly focuses on how to improve its microhardness and the abrasive resistance of the coatings [29-31]. However, studies into the corrosion resistance of cladding coatings with TiB phase are limited. Herein, the TiB composite coatings were successfully fabricated by an *in-situ* reaction and laser cladding technology, with the addition of differing concentrations of CeO_2 . The effects of the preplaced powder concentrations of CeO_2 on the microstructure, microhardness and corrosion resistance of the TiB-reinforced Ti cladding coatings were investigated.

2. EXPERIMENTAL DETAILS

The Ti-6Al-4V alloy was used as a substrate. The chemical compositions (wt%) were 6.5 Al, 4.26 V, 0.22 Fe, 0.07 C, 0.03 N, 0.01 H and 0.14 O, with Ti making up the balance. The substrates were cut into diameters of 50 mm and thicknesses of 10 mm; then, they were ground and ultrasonically cleaned in acetone for the laser cladding. The components of the preplaced mixture powders contained Ti powder (50–100 μm , purity 99.2%), B powder (average size 0.5 μm , purity 99.9%) and CeO_2 powder (20–50 nm, purity 99%). These components were blended and placed on the surface of the Ti-6Al-4V alloy to form a powder layer with a thickness of 1 mm. Table 1 lists the components of the preplaced mixture powders.

The laser cladding was performed with an IPG-YLS-5000W fibre laser at an output power of 3000 W, a scanning speed of 5 mm/s, a spot diameter of 5.0 mm and a laser wavelength of 1075 ± 5 nm to make a single-track cladding layer. The concentrations of the CeO_2 powder in the preplaced mixture were 1, 2 and 3 wt% (C1, C2 and C3, respectively). The process was completed in an Ar environment to prevent an oxidation reaction in the molten pool.

The samples of the laser cladding coatings were cut, ground and then polished. The cross-sections of the samples were etched in a solution of HF:HNO₃ (at a ratio of 1:2). The phase structures were measured with an X-ray diffractometer (XRD) with a Cu K α radiation (X'Pert PRO PANalytical). The cross-sections of the microstructures and the chemical compositions of the cladding coatings were characterised with a scanning electron microscope (SEM, Hitachi S-3400N) combined with an energy-dispersive spectrometer (EDS). The microhardness profiles and the cross-sections of the cladding coatings were ascertained with an HXD-1000 tester under a load of 500 g and a dwell time of 15 s.

Finally, the electrochemical measurements were conducted with a PARSTAT4000 electrochemical workstation at room temperature in a 3.5 wt.% NaCl solution (artificial seawater). The tests were performed using a three-electrode setup, where a Pt electrode served as the counter electrode, a saturated calomel electrode as the reference electrode and the cladding coatings as the working electrodes. The area covered by the cladding coatings that was exposed to the NaCl water solution was 1.13 cm². The cladding coatings were soaked in the 3.5 wt% NaCl water solution for 30 min to obtain a stable open circuit potential (OCP). The polarization curves of the cladding coatings were ascertained at a scanning rate of 1 mV/s. Electrochemical impedance spectroscopy (EIS) was performed at the OCP of the cladding coatings in the frequency range of 10⁵ Hz to 10⁻² Hz.

Table 1. Chemical components of the cladding powders

Number of samples	Preplaced powders (wt%)
C1	89% Ti + 10% B + 1% CeO ₂
C2	88% Ti + 10% B + 2% CeO ₂
C3	87% Ti + 10% B + 3% CeO ₂

3. RESULTS AND DISCUSSION

3.1. XRD phase analysis

The XRD patterns of the laser cladding coatings are shown in Fig. 1. The α -Ti and TiB phases were clearly seen in the coatings, and the phase structure did not significantly change with the increasing concentration of CeO₂. The compound of Ce was not seen in the XRD patterns probably because the concentration of the element Ce in the cladding coating was less, and the CeO₂ decomposed during the laser cladding. Subsequently, the active Ce atoms could easily react with the Ti atoms to generate intermetallics. Zhang et al. [32] studied laser cladding coatings with TiC, Ni and Y₂O₃ powders on a Ti alloy, and the element Y was similarly not detected in the XRD patterns due to its reduced concentration in the cladding coatings.

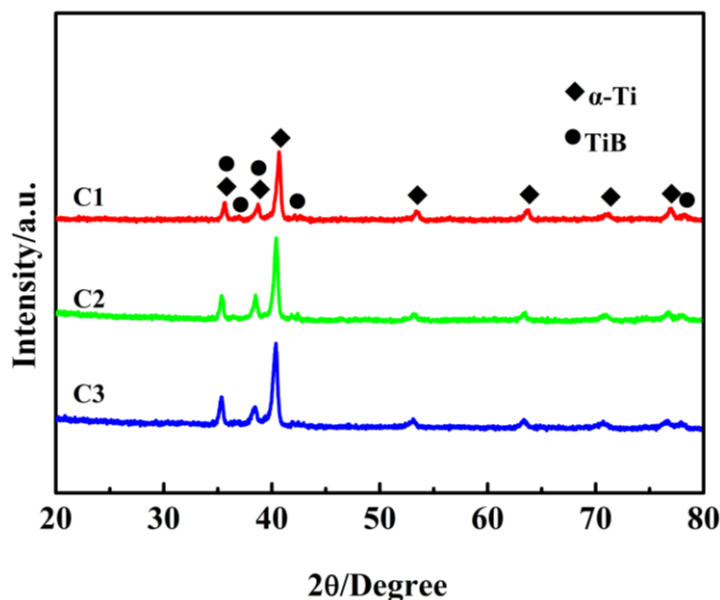


Figure 1. XRD patterns of the cladding coatings with different CeO₂ concentrations

3.2. Microstructure and morphology

Fig. 2 shows the SEM complete images from the cross-sections of the cladding coatings. The composite coatings presented a crescent shape after the laser cladding. This phenomenon occurred because the energy density of the IPG YLS-5000w fibre laser used in this experiment was of Gaussian distribution, thereby showing a high energy density in the centre of the laser and low energy density on both sides. When the laser beam acted on the surface of the preset coating, the irradiation energy at the centre of the laser beam was higher than that at the edge, thus resulting in a horizontal temperature gradient and a surface tension gradient. However, heat was transferred to the matrix by conduction. Given that the area in contact with the centre of the laser beam received higher energy, the matrix in the central region first melted. When the laser beam was swept, the molten pool was in a state of extreme cooling; accordingly, it retained its original crescent shape. Fig. 1 shows that high-quality metallurgical bonding occurred between the cladding coating and the substrate after the laser cladding, and no obvious cracks were observed in the cladding coatings. The thickness of the coatings decreased with the increase in the CeO₂ concentration and could be found by comparing the cladding coatings of C1, C2 and C3. The main reasons for this phenomenon are as follows. On the one hand, the addition of the Ce element improved the fluidity of the liquid metal in the molten pool, thereby promoting the elimination of bubbles in the molten pool and improving the density of the composite coating. On the other hand, the system can absorb additional energy with the increasing CeO₂ concentration, thereby further promoting the refinement of the microstructure.

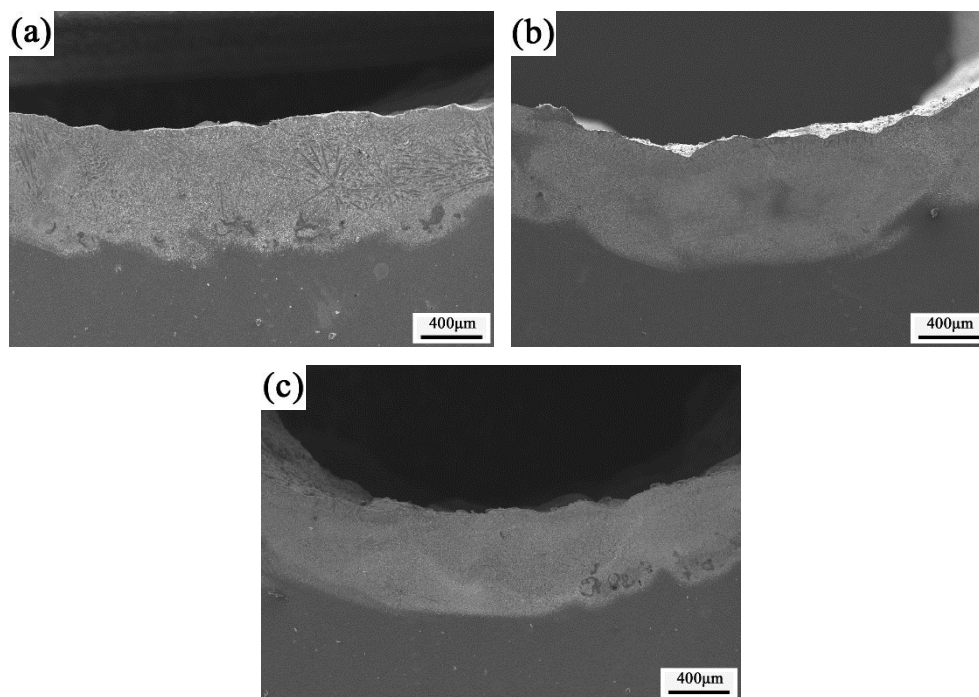


Figure 2. SEM images of the cladding coatings from the cross-sections of (a) C1, (b) C2 and (c) C3

Fig. 3 shows the SEM morphologies of the surface of the cladding coatings. Fig. 4 demonstrates the compositions of the different particles in the cladding coating obtained by EDS elemental analysis. The results are listed in Table 2. The black fishbone dendrite-shaped and the white needle-like particles mainly existed in the coatings with different CeO_2 concentrations. The EDS result showed that the components of the fishbone dendrite-shaped particles were mainly element Ti, and the white needle-like particles were elements Ti and B. The XRD and EDS analyses were combined, and the results indicated that the black fishbone dendrite-shaped phase was α -Ti (shown by B in Fig. 4 and Table 2), and the white needle-like phase was the reinforcement phase of the TiB (shown by A and C in Fig. 4 and Table 2). The length of the reinforcement phase of the TiB was short because it could not completely grow into a long rod after nucleation because the cooling rate on the surface of the coating was relatively quick. The magnified morphologies are shown in the insets of each picture in Fig. 3. The size of the black fishbone dendrite-shaped phase of the α -Ti in the coating decreased with the increase in the amount of CeO_2 ; however, the amount of the white needle-like phase of the TiB increased with the increase in the amount of CeO_2 . Fig. 3(c) shows that the grains were refined, and a large number of TiB particles appeared in the coating of the C3 sample. The two reasons for this phenomenon are as follows. First, Ce gathered around the grain boundaries, thereby increasing the energy of the system and further refining the grains [26]. Moreover, the areas of the grain boundaries increased with the refinement of the grains, which greatly improved the nucleation rate. Second, the active Ce atoms could easily react with the Ti atoms to generate metallic compounds. In addition, the rare-earth elements could promote the flow of liquid metal in the molten pool, thus reducing the surface tension of the liquid phase and increasing the dispersion of the TiB in the cladding coatings. The EDS result indicated that some Al and V were

detected because the convection of the liquid metal was generated in the molten pool; thus, some elements, such as Ti, Al and V, entered into the molten pool and remained in the coating after cooling.

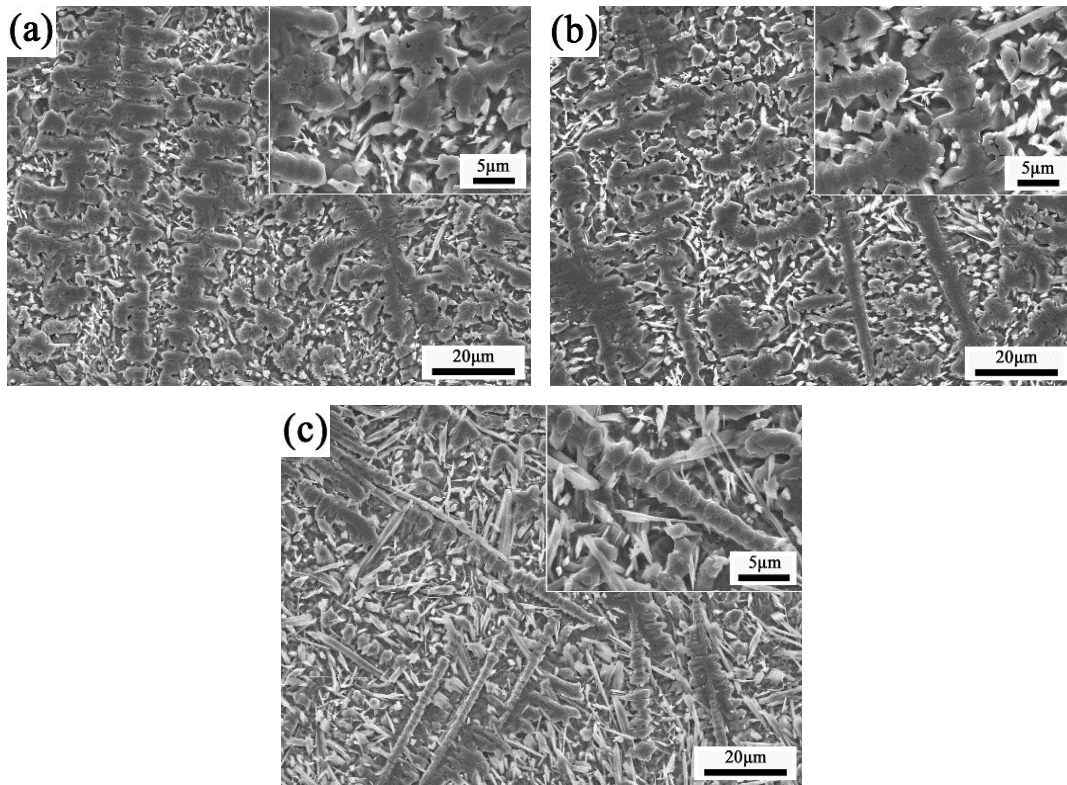


Figure 3. SEM morphologies of the surface of the cladding coatings: (a) C1, (b) C2 and (c) C3

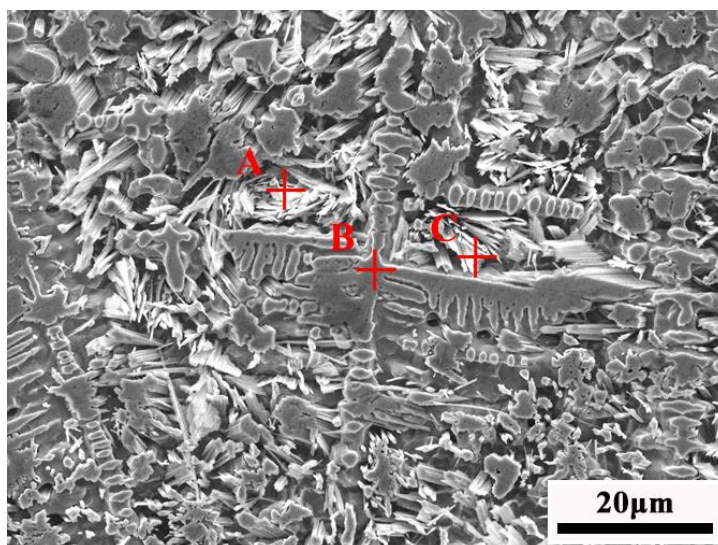


Figure 4. SEM morphology of the surface of the cladding coating of C3

Table 2. Compositions of different spots marked in Fig. 4

Spots	Elements (at%)					
	Ti	B	Ce	Al	O	V
A	47.69	39.35	3.25	0.84	6.53	2.32
B	95.33		1.45	1.33		1.89
C	53.20	34.35	3.73	1.59	4.71	2.42

The SEM morphologies of the centre of the cladding coatings are presented in Fig. 5. The size of the α -Ti phase in the centre of the coating was significantly smaller, and the amount was reduced, whilst the TiB phase simultaneously increased. During the rapid cooling of the molten pool, a longer cooling time was observed in the centre of the coating than on the surface; thus, the TiB had sufficient time to nucleate and grow. Furthermore, the fishbone dendrite-shaped phase of the α -Ti was rarely present, and the white needle-like phase of the TiB was refined in the centre of the C3 coating. This observation was similar to the surface of the coatings; the addition of the element Ce could increase the energy and activity of the system, thereby promoting grain refinement of the TiB.

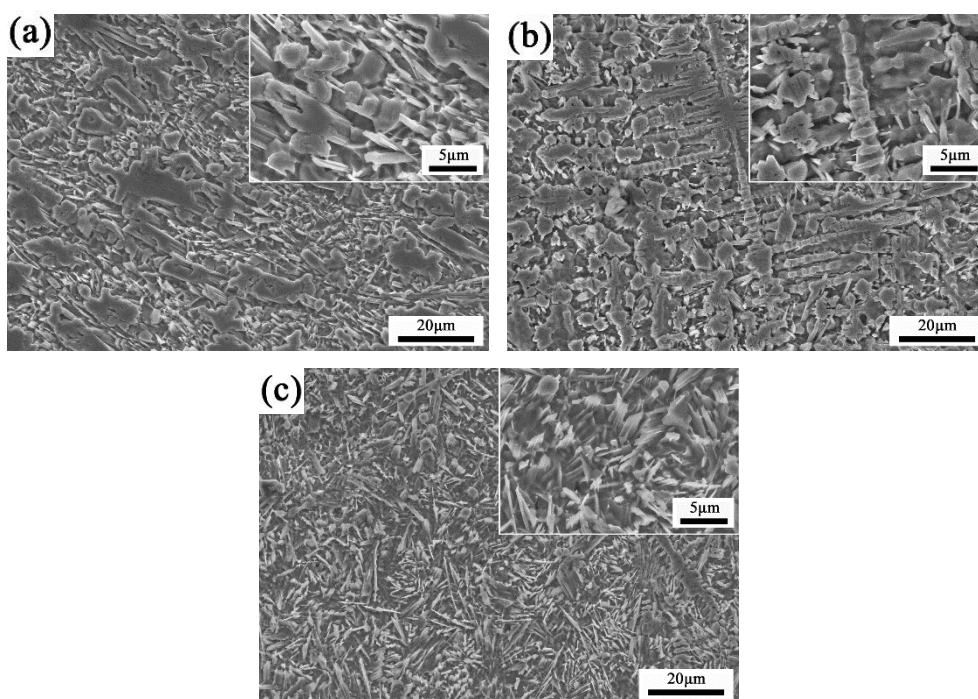


Figure 5. SEM images of the centre of the cladding coatings: (a) C1, (b) C2, and (c) C3

Fig. 6 shows the morphologies of the bottom of the coatings. The grains in the coatings with differing concentrations of CeO_2 uniformly distribute; the distribution of the grains is similar to a network and extends deep into the substrate, forming a good metallurgical bond. A clear boundary in the bonding zone of the cladding coatings could be seen; this situation was attributed to the direction of the

grain's growth, depending on the direction of the heat transfer in the high-temperature molten pool. During the laser cladding, the prefabricated coating absorbed a large amount of heat and rapidly melted. The heat energy was conducted downward, and a portion of the energy was absorbed by the surface of the substrate; accordingly, it began to melt. The grains could not sufficiently grow because the substrate had low undercooling. Accordingly, the microscopic grains were fine.

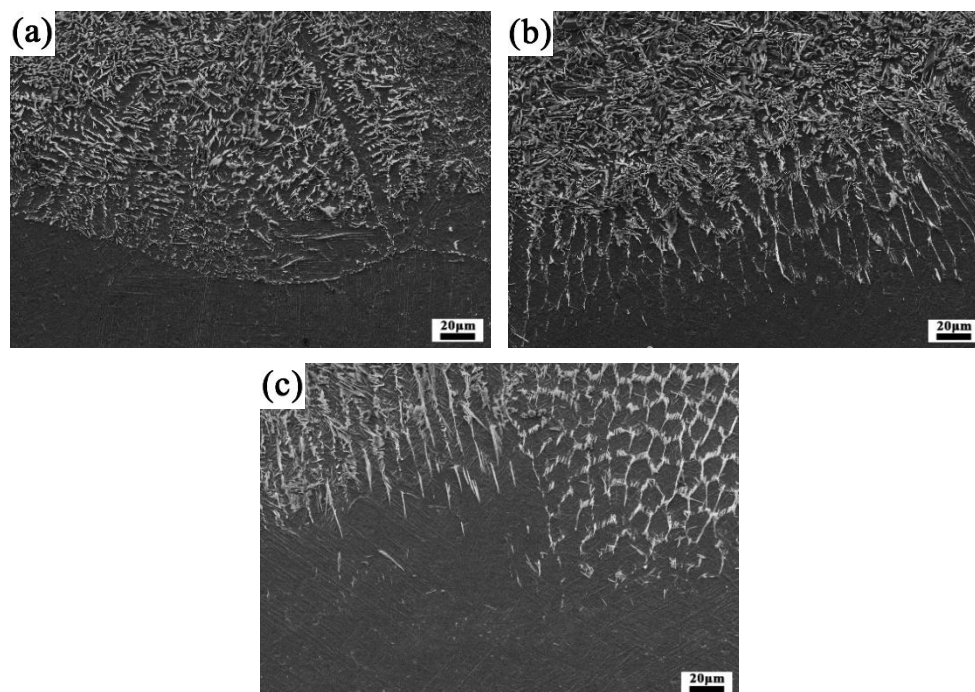


Figure 6. SEM morphologies of the bottom of the cladding coatings: (a) C1, (b) C2 and (c) C3

3.3. Microhardness

Fig. 7 shows the cross-sectional microhardness profiles of the composite coatings with different added concentrations of CeO_2 from the surface to the substrate. The microhardness was greater at the surface of the cladding coatings and gradually decreased with the increasing distance from the surface. The microhardness rapidly decreased in the bonding zone and then gradually stabilised at approximately 350 HV. The gradient variation of the microhardness in the coating was due to the change in the microstructure. The microhardness of the cladding coatings was significantly enhanced by the addition of a great concentration of CeO_2 . The microhardness of the cladding coatings increased by threefold or fourfold compared with that of the Ti-6Al-4V substrate because of the existence of the TiB's reinforcement phase. This phenomenon was principally attributed to the dispersed hardening by the TiB phase and the fine grain strengthening due to the addition of the rare-earth element (CeO_2). The microhardness of the cladding coatings increased with the increased concentration of the added rare-earth element Ce, which is coincident with the microstructure. The microhardness reached its maximum average value of 1044.6 HV when the added CeO_2 concentration was 3 wt% due to the rare-earth element promoting the uniformity and formation of a well-defined microstructure in the cladding coating. The

wear resistance of a material is related to its microhardness; accordingly, a great microhardness leads to a wear resistance of a material [33,34].

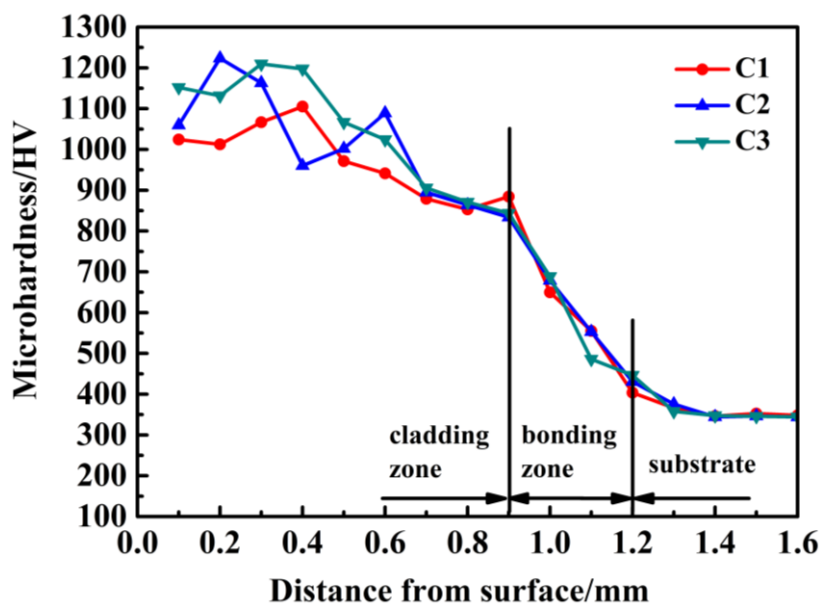


Figure 7. Microhardness of the laser cladding coatings

3.4. Corrosion

Fig. 8 shows the polarization curves of the samples in the 3.5 wt% NaCl solution. The corrosion potential (E_{corr}) and corrosion current density (I_{corr}) of the samples were measured by linear Tafel extrapolation and are shown in Table 3. In Fig. 8, the polarization curves of the cladding coatings move toward the bottom right corner. Fig. 8 and Table 3 demonstrate that the E_{corr} for all the laser cladding coatings was higher than that of the substrate (-606 mV). Meanwhile, the I_{corr} for all the laser cladding samples was lower than that of the substrate ($0.0116 \mu\text{A}/\text{cm}^2$).

After laser treatment, the E_{corr} of the C3 sample increased to -403 mV, and the I_{corr} reduced to $0.0022 \mu\text{A}/\text{cm}^2$. The cladding coating of the C3 sample was rich in the reinforced TiB phases, which were uniformly distributed in the cladding coating. Thus, the cladding coating was more stable with a higher E_{corr} . An appropriate concentration of Ce can increase the nucleation rate, thereby effectively promoting grain refinement. The grains with an ultrafine structure on the surface of the cladding coating can form a stable protective film.

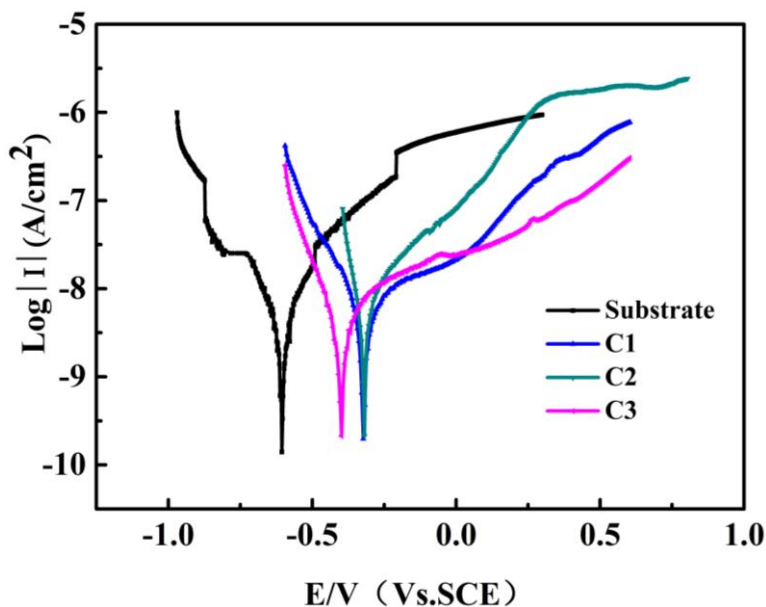


Figure 8. Polarization curves for the cladding coatings exposed 1.13 cm² in the 3.5 wt% NaCl solution at 1 mV/s

Table 3. Corrosion potential and current density of the samples

Samples	E _{corr} (mV)	I _{corr} (μA/cm ²)
Substrate	-606	0.0116
C1	-323	0.0052
C2	-324	0.0049
C3	-403	0.0022

The electrochemical impedance experiments of the samples were conducted in a 3.5% NaCl solution. The radius of the resistance arc represents the value of the polarization resistance (R_p) of a sample (i.e. the corrosion resistance is good when the radius of the resistance arc is large). Fig. 9(a) shows that the radius of the resistance arc increased with the increase in the CeO₂ concentration. The laser cladding TC4 alloy coating had a better corrosion resistance than the substrate, and the C3 sample was the best. Figs. 9(b) and 9(c) show the Bode plots for modulus $|Z|$ versus frequency and the phase angle versus frequency.

The high-frequency region (from 10³ to 10⁵ Hz) of the Bode plots for the impedance modulus, $|Z|$, versus frequency shows the electrolyte impedance between the samples and the reference electrode; by contrast, the low-frequency region (from 10⁻² to 10⁰ Hz) corresponds to the polarization resistance (R_p) of the samples shown in Fig. 9(b) [35-36]. The impedance modulus, $|Z|$, of the cladding coatings increased with the increase in CeO₂ concentrations in the low-frequency region. Moreover, the impedance modulus, $|Z|$, of the C3 sample was always the largest; this finding indicates that it exhibited

the best overall corrosion resistance. In Fig. 9(c), the phase angle values reduced to zero in the high-frequency region (from 10^3 to 10^5 Hz). In the medium- to low-frequency range (from 10^{-2} to 10^3 Hz), the phase angle values approached 70° , thereby showing an obvious near-capacitive behaviour of all the samples after immersion in a corrosive medium. The region at the high-phase angle ($>60^\circ$) for the C1, C2 and C3 samples was wider than that of the substrate. The C1, C2 and C3 samples displayed a comparatively steady surface state in our test.

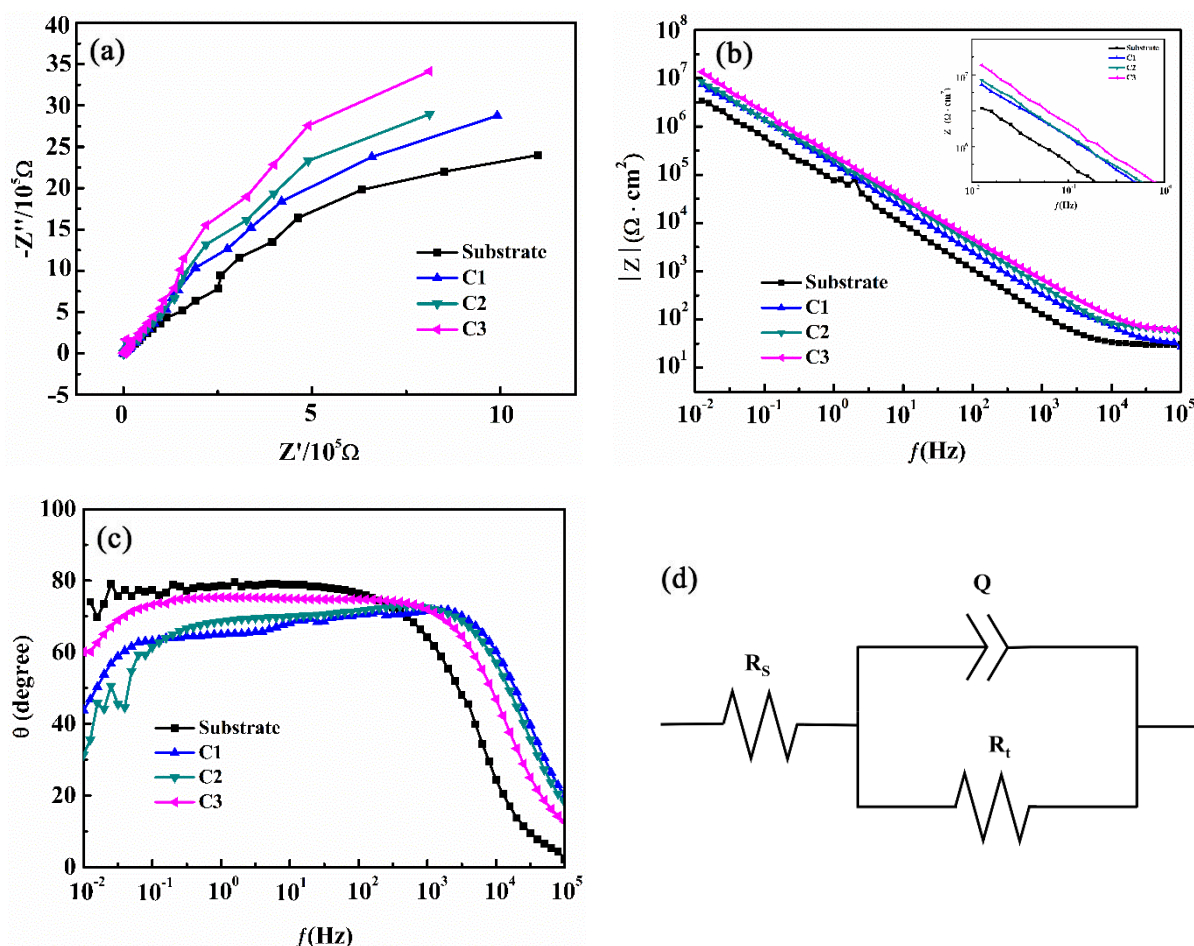


Figure 9. EIS results for the samples exposed to 1.13 cm^2 in the 3.5 wt% NaCl water solution at 1 mV/s: (a) Nyquist plot, (b) Bode plots for modulus $|Z|$ versus frequency, (c) Bode plots for the phase angle versus frequency and (d) equivalent circuit proposed for fitting the EIS plots

To provide an accurate theoretical analysis of the EIS, the equivalent circuit is shown in Fig. 9(d). In this equivalent circuit (Fig. 9(d)), R_s corresponds to the solution resistance, and R_t denotes the charge transfer resistance when the electrode reacts. Furthermore, the capacitive responses were fitted by constant-phase angle elements (CPE) Q , and its impedance is defined as follows:

$$Z_Q = \frac{1}{Y_0} \cdot (j \cdot \omega)^{-n}, \quad (1)$$

where Y_0 is the CPE constant, j is the imaginary unit ($j = \sqrt{-1}$), ω is the angular frequency ($\omega = 2\pi f$, where f is the frequency), and fractional exponent n is the CPE parameter [37].

In this process, the electrode potential (E) is the only variable state that determines the speed of the electrode process. Accordingly, the expression for estimating the polarization resistance (R_p) is as follows:

$$R_p = R_t. \quad (2)$$

The results of fitting the EIS data by using the equivalent circuit are shown in Table 4. The maximum R_p ($R_p = R_t$) of $2.206 \times 10^{17} \Omega \cdot \text{cm}^2$ was obtained for coating C3, thereby indicating that it had an optimal overall corrosion resistance. The R_p of the laser cladding coatings increased with the increase in CeO_2 concentrations. This phenomenon occurred because the TiB particles were refined, and the cladding coatings were reinforced with the increasing CeO_2 concentrations, which led to the improved corrosion resistance of the laser cladding coatings. This result agrees with the above-mentioned polarization curve.

Table 4. Fitted EIS data based on the equivalent circuits presented in Figure 9(d)

Samples	R_s ($\Omega \cdot \text{cm}^2$)	Y_{0dl} ($\Omega^{-1} \cdot \text{cm}^{-2} \cdot \text{s}^{-n}$)	n_{dl}	R_t ($\Omega \cdot \text{cm}^2$)
Substrate	29.37	2.309×10^{-6}	0.9255	2.017×10^7
C1	37.5	1.234×10^{-6}	0.8574	8.121×10^{14}
C2	44.13	9.781×10^{-7}	0.8558	5.758×10^{16}
C3	56.43	8.211×10^{-7}	0.8584	2.206×10^{17}

4. CONCLUSION

In this study, laser cladding surface modification was applied to a Ti-6Al-4V alloy by using Ti/B/CeO₂ powder to study the effect of different CeO₂ concentrations on the phase composition, microstructure, microhardness and corrosion of the cladding coatings. The coatings comprised black fishbone-shaped α -Ti dendrites and white needle-like TiB particles when a laser scanning speed of 5 mm/s and a laser power of 3.0 kW were used. The cladding coating and the substrate metallurgically combined well after the laser cladding, and no obvious cracks were found in the cladding coatings. The thickness of the coatings decreased with the increase in CeO₂ concentrations in the coatings. The addition of CeO₂ also promoted the formation of a uniform and refined microstructure of the cladding coatings, and a well-defined structure was achieved when the CeO₂ concentration was 3 wt.%. The microhardness of the cladding coatings with added differing concentrations of CeO₂ was threefold or fourfold greater than that of the Ti alloy substrate and achieved a maximum average of 1044.6 HV for C3. The corrosion properties were significantly improved by the addition of CeO₂ into the coatings. The E_{corr} for all the laser cladding samples was higher than that of the substrate (-606 mV), and the I_{corr} for all the laser cladding samples was lower than that of the substrate ($0.0116 \mu\text{A}/\text{cm}^2$). The R_p of the laser cladding coatings increased with the increase in CeO₂ concentrations, and a maximum R_p of $2.206 \times 10^{17} \Omega \cdot \text{cm}^2$ was obtained for coating C3. In summary, the optimal corrosion resistance of the cladding coating was achieved with the addition of a 3 wt% concentration of CeO₂.

ACKNOWLEDGEMENTS

This work was supported by the Nature Science Foundation of China (No. 51701114, 11604204 and 51603120).

References

1. F. Weng, C. Chen and H. Yu, *Mater. Design.*, 58 (2014) 412.
2. Y. Lin, Y. Lei, X. Li, X. Zhi and H. Fu, *Opt. Laser. Eng.*, 82 (2016) 48.
3. I. Gurrappa and A. K. Gogia, *Surf. Coat. Tech.*, 139 (2001) 216.
4. Y. Lin, J. Yao, Y. Lei, H. Fu and L. Wang, *Opt. Laser. Eng.*, 86 (2016) 216.
5. R. G. Henning, D. R. Bouchet, J. Srinivasan, S. G. Albers, C. Robert and J. W. Wilkins, *Nat. Mater.*, 4 (2005) 129.
6. S. Wang, *Int. J. Electrochem. Sci.*, 13 (2018) 6414.
7. H. K. S. Rahomaa, Y. Y. Chen, X. P. Wang and S. L. Xiao, *J. Alloy. Compd.*, 627 (2015) 415.
8. X. L. Guo, L. Q. Wang and M. M. Wang, *Acta. Mater.*, 60 (2012) 2656.
9. W. Wang, *Int. J. Electrochem. Sci.*, 14 (2019) 2224.
10. G. Huang, X. Guo, Y. Han, L. Wang, W. Lu and D. Zhang, *Mat. Sci. Eng. A.*, 667 (2016) 317.
11. M. Li, J. Huang, Y. Y. Zhu and Z. G. Li, *Surf. Coat. Tech.*, 206 (2012) 4021.
12. J. Li, C. Chen and J. Hu, *Surf. Interface. Anal.*, 44 (2012) 559.
13. O. F. Ochonogor, C. Meacock, M. Abdulwahab, S. Pityana and A. P. I. Popoola, *Appl. Surf. Sci.*, 263 (2012) 591.
14. J. Z. Shao, J. Li, R. Song, L. L. Bai and C. C. Qu, *Rare Metals*, 7 (2016) 1.
15. Q. Li, Y. Lei, and H. Fu, *Surf. Coat. Tech.*, 239 (2014) 102.
16. L. Ding, S. Hu, X. Quan and J. Shen, *Appl. Phys. A-Mater.*, 122 (2016) 288.
17. Y. B. Guo, Z. G. Li, C. W. Yao, K. Zhang, F. G. Lu, K. Feng, J. Huang, M. Wang, Y. X. Wu, *Mater Design*, 63 (2014) 100.
18. Y. Li, F. Xie, X. Wu and X. Li, *Appl. Surf. Sci.*, 287 (2013) 30.
19. M. X. Li, Y. Z. He and X. M. Yuan, *Appl. Surf. Sci.*, 258 (2006) 2882.
20. M. X. Li, S. H. Zhang, H. S. Li, Y. Z. He, J. H. Yoon and T. Y. Cho. *J. Mater. Process. Tech.*, 202(2008) 107.
21. P. Q. Xu, X. H. Tang, S. Yao, J. P. He and G. X. Xu, *J. Mater. Process. Tech.*, 208 (2008) 549.
22. C. Liu, R. I. Revilla, Z. Y. Liu, D. W. Zhang, X. G. Li and H. Terryn. *Corros. Sci.*, 129 (2017) 82.
23. Y. Wei, C. Q. Zheng, P. Fan, S. H. Cheng, W. Li and G. F. Ying, *J. Alloy. Compd.*, 311 (2000) 65.
24. X. H. Zhang, C. Zhang, Y. D. Zhang, S. Salam, H. F. Wang and Z. G. Yang, *Corros. Sci.*, 88 (2014) 405.
25. J. N. Li, H. J. Yu, S. L. Gong, C. Z. Chen, F. Weng, L. Ding, Y. K. Pan and F. H. Shan, *Surf. Coat. Tech.*, 247 (2014) 55.
26. D.H. Lu, S. S. Liu, X. Y. Zhang and W. P. Zhang, *Surf. Interface. Anal.*, 47 (2014) 239.
27. B. Courant, J. Hantzpergue and S. Benayoun, *Wear*, 236 (1999) 39.
28. H. Zhang, Y. Zou, Z. D. Zou and C. W. Shi, *J. Rare. Earth.*, 32 (2014) 1095.
29. A. Qi, L. J. Huang, S. Jiang and X. T. Li, *Vacuum*, 145 (2017) 312.
30. L. F. Cai, Y. Z. Zhang and L. K. Shi, *Rare Metals*, 26 (2007) 342.
31. J. Z. Shao, J. Li, R. Song, L. L. Bai, J. L. Chen and C.C. Qu, *Rare Metals*, 7 (2016) 1.
32. K. M. Zhang, J. X. Zou, J. Li, Z. S. Yu and H. P. Wang, *Trans. Nonferrous Met. Soc. China.*, 22 (2012) 1817.
33. H. M. Wang and Y. F. Liu, *Mat. Sci. Eng. A.*, 338 (2002) 126.
34. Y. F. Liu, Y. L. Zhou, Q. Zhang, F. Pu, R. H. Li and S. Z. Yang, *J. Alloy. Compd.*, 591 (2014) 251.
35. F. L. Floyd, S. Avudaiappan, J. Gibson, B. Mehta, P. Smith and T. Provder and J Escarsega, *Prog. Org. Coat.*, 66 (2009) 8.

36. A. Nishikata, Y. Ichihara and T. Tsuru, *Corros. Sci.*, 37 (1995) 897.
37. P. Zoltowski, *J. Electroanal. Chem.*, 443 (1998) 149.

© 2021 The Authors. Published by ESG (www.electrochemsci.org). This article is an open access article distributed under the terms and conditions of the Creative Commons Attribution license (<http://creativecommons.org/licenses/by/4.0/>).